*J. Fluid Mech.* (2001), *vol.* 442, *pp.* 191–215. Printed in the United Kingdom



# Numerical investigations of heat transfer mechanisms in the forced laminar wall jet

By JÜRGEN SEIDEL AND HERMANN F. FASEL

Department of Aerospace and Mechanical Engineering, University of Arizona, Tucson, AZ 85721, USA

(Received 18 February 1999 and in revised form 19 December 2000)

The effect of high-amplitude forcing on a laminar wall jet over a heated flat plate is analysed. Highly accurate direct numerical simulations (DNS) are used to investigate the dominant transport mechanisms. When forcing is applied, the skin friction is reduced markedly and the wall heat transfer is increased. Detailed examination of the unsteady flow field showed that the concepts of eddy viscosity and eddy thermal diffusivity, usually applied to turbulent flows, can be applied to the analysis of unsteady laminar flows to explain the effect of highly unsteady phenomena.

## 1. Introduction

A wall jet is the flow that develops when a fluid is blown tangentially along a wall. Wall jets have many important technical applications such as boundary layer control and lift enhancement on airfoils by making use of their tendency to adhere to surfaces (Coanda effect). Probably the most common application of a wall jet involving heat transfer is the windshield defroster system in automobiles, where a jet of hot air is blown along the windshield to affect mass transfer from and heat transfer to the surface. Other applications in which a wall jet is used to cool and protect surfaces from hot and/or corrosive fluids range from the cooling of turbine blades and combustion chamber walls to the cooling of the outer surfaces in high-speed vehicles or rockets (Launder & Rodi 1983). Recently, cooling of electronic components has become increasingly important.

Irrespective of its application, a wall jet acts as a source of momentum and as a source or sink of heat. The jet may be issued into coflowing, quiescent, or counterflowing surroundings. The external stream may be accelerating or decelerating such as in airfoil or turbine blade applications. In addition, the external flow can be laminar or turbulent. The surface itself might be smooth, rough, or even highly irregular, such as in electronic cooling applications.

Despite this variety of important technical applications, the wall jet, its hydrodynamic stability characteristics, especially the nonlinear stages, as well as the influence of unsteadiness on the mean surface shear stress and heat transfer has only recently been investigated more closely.

The first investigation of the incompressible wall jet was reported by Tetervin (1948). He predicted a growth of the wall jet thickness proportional to $x^{3/4}$, and a corresponding decay in maximum jet velocity of $x^{-1/2}$ ($x$ is the coordinate in the streamwise direction). Closed form solutions of the boundary layer equations for the wall jet geometry were published by Akatnov (1953) and Glauert (1956). Experimental verification of these theoretical findings was given by Bajura & Szewezyk (1970). Their

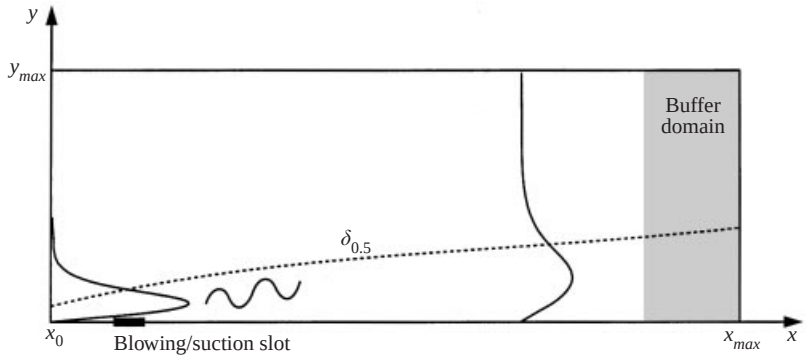


FIGURE 1. Computational domain with blowing/suction slot for disturbance generation.

results were substantiated by Gorla & Jeng (1971), who performed an analysis based on integral methods. Recently, Cohen, Amitay & Bayly (1192) investigated the wall jet subjected to blowing or suction from the surface. They found a family of similarity solutions which include Glauert's result for the case of zero blowing. These theoretical findings were later verified experimentally by Amitay & Cohen (1993).

The hydrodynamic stability of the wall jet was first studied by Chun & Schwarz (1967). By solving the Orr–Sommerfeld equation (temporal approach), they predicted a critical Reynolds number of 57 (based on the local maximum jet velocity and the jet half-width, see figure 1 in § 2). They also showed the existence of two unstable eigenmodes, one associated with the viscous instability in the inner region and the other with the inviscid instability of the shear layer in the outer region. Furthermore, they found a region of stability between the Reynolds numbers of 370 and 750, inside the unstable region. Tsuji *et al.* (1977) were able to confirm these findings, both experimentally and numerically (solving the Orr–Sommerfeld equation). Bajura & Szewezyk (1970) determined the amplitude distribution of the disturbances of the streamwise velocity experimentally and found that it has three distinct peaks, one in the inner region, one in the outer region with the maximum near the inflection point of the mean velocity profile, and a weaker peak further away from the wall.

Bajura & Catalano (1975) investigated the whole transition process of a wall jet in a water tunnel. Using flow visualization techniques, they found the following five stages for both natural and forced transition: (i) formation of vortices in the free shear layer, (ii) vortex merging, resulting in a disturbance signal of half the imposed frequency, (iii) eruption of the wall jet into the ambient fluid, (iv) onset of three-dimensional motion and turbulence, (v) relaminarization until the next vortex merging. The early stages of this process were found to be highly two-dimensional, with a ratio of the spanwise length of vortex filaments to the local boundary layer thickness as large as 50 : 1, indicating that the transition process is governed by the shear layer instability. This notion was further subtantiated by the absence of turbulent spots near the wall, which are typical in boundary layer transition.

The existence of two unstable modes was clarified by Mele *et al.* (1986). They were able to show that one mode, unstable at low disturbance frequencies, is in fact associated with the inflection point in the free shear layer. The other mode, unstable with respect to higher frequencies, is due to the boundary layer type, viscous instability. A very detailed map of these two modes was given by Wernz (1993). Zhou, Rothstein

& Wygnanski (1992) successfully matched their experimental data with the theoretical predictions of linear stability theory in different regions of the stability diagram.

Using particle image velocimetry (PIV) and laser visualization techniques, Gogineni, Visbal & Shih (1997) investigated the transitional wall jet. They were able to confirm the existence of a double row of discrete vortices, associated with the inner and outer regions of the wall jet. Their findings were substantiated by Amitay (1994), who used dye injection techniques in a water tunnel to visualize the vortical structures. In addition, he observed the vortex pairing and the highly two-dimensional structure of the wall jet in the early stages of transition, confirming the results of Bajura & Catalano (1975). In a later study, Amitay & Cohen (1997) investigated the stability of a wall jet subjected to blowing or suction. They found that net wall blowing increases the ratio between the outer and inner amplitude maximum of the streamwise velocity fluctuations, while wall suction has the opposite effect. Furthermore, wall blowing or suction has a significant effect on the stability of the wall jet.

Recently, Wernz & Fasel (1996, 1997) studied the transition process of the wall jet numerically, for both two-dimensional and three-dimensional disturbances. When forced at high disturbance amplitudes, the skin friction was markedly reduced. If forcing at even higher amplitudes was introduced, mushroom shaped vortex pairs are ejected into the ambient fluid. They found that the onset of this phenomenon is highly dependent on the initial conditions and conjectured that this phenomenon might be chaotic in nature. For the three-dimensional case, they found both two- and three-dimensional subharmonic resonances, while the three-dimensional fundamental resonance was found to be only weak. They concluded that the subharmonic resonance can be supressed if three-dimensional disturbances of large enough amplitude are introduced. On the other hand, when random three-dimensional forcing was introduced, they saw the emergence of vortical structures with strong spanwise coherence, but these structures were not ejected into the ambient fluid.

For the wall jet with heat transfer, Schwarz & Caswell (1961) found a self-similar solution, assuming constant fluid properties. Gorla & Jeng (1971) extended their analysis of the laminar wall jet for Prandtl number ranging from 0.01 to 1000. Recently, Likhachev & Tumin (1996) investigated the stability of a compressible laminar wall jet with heat transfer. In the incompressible limit, linear stability theory predicts a significant change in the range of unstable frequencies for large temperature differences between wall and ambient. However, the critical Reynolds number remains practically unchanged.

From the discussion above it becomes obvious that the investigation of the stability of the laminar wall jet, especially the nonlinear stages, is still in its infancy when compared to the abundance of information available about boundary layer transition. The effects of heat transfer on the wall jet stability are even less understood. From experiments, calculations and theoretical work on boundary layers it is known that the heat transfer characteristics change significantly when the flow transitions from the laminar to the turbulent flow regime. Without reliable knowledge of the transition location, one is unable to predict the temperature of the surface, even if only a rough estimate is sought.

So far, the Reynolds analogy

$$\tfrac{1}{2}C_f = StPr^{2/3}, \tag{1.1}$$

where $c_f$ is the skin friction coefficient, $St$ is the Stanton number, and $Pr$ is the Prandtl number, has been used to predict the heat transfer characteristics of wall-bounded flows. This analogy takes advantage of the similarity between the momentum and

energy equations when the boundary layer assumptions are made. However, the applicability of this analogy for highly unsteady flows is questionable, as discussed below.

For the computation of the mean flow velocity and temperature distribution of turbulent flows, eddy viscosity models have been proposed. The eddy viscosity $\nu_t$ is defined as

$$\overline{u'v'} = -\nu_t \frac{\partial \bar{u}}{\partial y}. \tag{1.2}$$

Similarly, a thermal eddy diffusivity $\kappa_t$ can be defined as

$$\overline{v'T'} = -\kappa_t \frac{\partial \bar{T}}{\partial y}. \tag{1.3}$$

The total viscosity is then $\nu + \nu_t$ and the total thermal diffusivity $\kappa + \kappa_t$. In general, both $\nu_t$ and $\kappa_t$ are functions of position.

Introducing these quantities into the Reynolds analogy yields $\nu_t = \kappa_t$ (if $Pr = 1$). From the reduction of skin friction found experimentally and numerically for the forced isothermal wall jet, therefore, a reduction of the wall heat flux could be anticipated.

Holmberg & Pestian (1996) investigated an unforced turbulent wall jet and observed an increase in wall heat transfer in the presence of high free-stream turbulence. Examining velocity–temperature correlations, they concluded that the large-scale motion in the flow is the driving force. Also, Dec & Keller (1990) found that the heat transfer is always enhanced by large, unsteady structures, indicating a breakdown of the Reynolds analogy for unsteady wall jets.

In this paper, an attempt is made to clarify the role of the unsteady, large structures in the heat transfer from the wall in a wall jet. Highly accurate direct numerical simulations (DNS) are used to investigate the laminar wall jet subject to external, periodic forcing at different amplitude levels. The focus is on the effect of the large structures on the mean flow quantities such as wall skin friction and wall heat transfer.

For code validation, the numerical results are compared to results from linear stability theory. Next, the effect of large-amplitude forcing on the skin friction as well as the wall heat transfer is investigated. The effectiveness of various forcing frequencies and amplitudes is explored, with focus on skin friction reduction and heat transfer increase/reduction at high amplitude levels.

With these results, a detailed analysis of the effects of the unsteady structures in the flow is possible, especially the influence of these structures on the wall heat transfer. By comparing the eddy diffusivity with the mean temperature profiles, a clearer picture of the processes affecting the mean flow quantities can be developed.

This investigation of the forced laminar wall jet is an essential step towards the understanding of transitional and turbulent wall jets. In the turbulent wall jet, highly energetic small structures are present, so that the questions posed above have to be addressed again. However, with the knowledge gained from the investigation of the laminar wall jet, it should be much easier to identify the relevant turbulent mechanisms and their influence on the wall heat transfer.

## 2. Numerical model

### 2.1. *Governing equations*

The governing equations are the two-dimensional, incompressible, unsteady Navier–Stokes equations in vorticity–velocity formulation and the energy equation. The

velocity components in the streamwise ($x$) and wall normal ($y$) directions are $u$ and $v$, respectively (figure 1).

In these equations, the velocities are normalized by the jet exit velocity $U_j$, the spatial variables $x$, $y$ by the nozzle width $b$, the time by $b/U_j$, and the temperature by the temperature of the free stream $T_\infty$.

By taking the curl of the momentum equations, the pressure gradient terms are eliminated and the following transport equation for the spanwise component of the vorticity ($\omega_z$) can be obtained:

$$\frac{\partial \omega_z}{\partial t} = -\frac{\partial c}{\partial x} + \frac{\partial b}{\partial y} + \frac{1}{Re}\nabla^2 \omega_z, \tag{2.1}$$

where

$$b = -v\omega_z - \frac{\partial \tau'_{xx}}{\partial x} - \frac{\partial \tau'_{xy}}{\partial y}, \quad c = u\omega_z - \frac{\partial \tau'_{xy}}{\partial x} - \frac{\partial \tau'_{yy}}{\partial y}. \tag{2.2a,b}$$

with $\tau'_{ij} = (v(T) - v_\infty)/Re(u_{i,j} + u_{j,i})$ and $\nabla^2 = \partial^2/\partial x^2 + \partial^2/\partial y^2$. The global Reynolds number is defined as $Re = U_j b/v_\infty$.

The vorticity is defined as

$$\omega_z = \frac{\partial u}{\partial y} - \frac{\partial v}{\partial x}, \tag{2.3}$$

and the Poisson equations for the velocity components are

$$\nabla^2 v = -\frac{\partial \omega_z}{\partial x}, \tag{2.4a}$$

$$\frac{\partial^2 u}{\partial x^2} = -\frac{\partial^2 v}{\partial x \partial y}. \tag{2.4b}$$

The energy equation is written with the temperature as the dependent variable,

$$\frac{\partial T}{\partial t} = \frac{\partial d}{\partial x} + \frac{\partial e}{\partial y} + \frac{1}{Pe}\nabla^2 T, \tag{2.5}$$

where

$$d = -Tu + \frac{\kappa'(T)}{Pe}\frac{\partial T}{\partial x}, \quad e = -Tv + \frac{\kappa'(T)}{Pe}\frac{\partial T}{\partial y}, \tag{2.6a,b}$$

$\kappa' = \kappa(T) - \kappa_\infty$, and $Pe = RePr = U_j b/\alpha_\infty$.

To model the temperature dependence of the viscosity and the thermal conductivity of air, fourth-order polynomial fitting to experimental data was chosen (Bertolotti 1991),

$$\mu = \mu_0 + \mu_1 T + \mu_2 T^2 + \mu_3 T^3 + \mu_4 T^4, \tag{2.7a}$$

$$\kappa = \kappa_0 + \kappa_1 T + \kappa_2 T^2 + \kappa_3 T^3 + \kappa_4 T^4, \tag{2.7b}$$

with

$$\begin{aligned}
&\mu_0 = -1.561632014 \times 10^{-7}, \quad \kappa_0 = -1.305884703 \times 10^{-3},\\
&\mu_1 = 7.957989891 \times 10^{-8}, \quad \kappa_1 = 1.099134492 \times 10^{-4},\\
&\mu_2 = -6.930149679 \times 10^{-11}, \quad \kappa_2 = -6.846979087 \times 10^{-8},\\
&\mu_3 = 4.068157752 \times 10^{-14}, \quad \kappa_3 = 3.327083322 \times 10^{-11},\\
&\mu_4 = -9.182486030 \times 10^{-18}, \quad \kappa_4 = -5.397866355 \times 10^{-15}.
\end{aligned}$$

### 2.2. *Boundary conditions*

The governing equations (2.1), (2.4), (2.5) are solved in the computational domain shown in figure 1. At the inflow boundary $x = x_0$, all velocity and vorticity components as well as the temperature are specified. In all cases presented here, these inflow conditions are obtained from the similarity solution of the wall jet over a heated wall where the jet fluid has the same temperature as the ambient fluid (Likhachev, Quintana & Wygnanski 1998). At the wall $y = 0$, the no-slip condition is imposed on the $u$-velocity. The normal velocity $v$ is zero except at the disturbance slot, where a $v$-velocity distribution is specified such that mass-neutral, periodic blowing and suction is possible to introduce disturbance waves into the flow (Fasel, Rist & Konzelmann 1990),

$$v(x,t) = \hat{v} v_s(x) \cos(\omega t), \tag{2.8}$$

where $\hat{v}$ is the amplitude, $\omega$ the circular frequency, and $v_s(x)$ is the shape function over the disturbance slot,

$$x_1 \leqslant x \leqslant x_c : v_s(\xi) = \tfrac{1}{48}(729\xi^5 - 1701\xi^4 + 972\xi^3), \quad \xi = \frac{x - x_1}{x_c - x_1}, \tag{2.9a}$$

$$x_c \leqslant x \leqslant x_2 : -v_s(\xi) = \tfrac{1}{48}(729\xi^5 - 1701\xi^4 + 972\xi^3), \quad \xi = \frac{x_2 - x}{x_2 - x_c}. \tag{2.9b}$$

The wall temperature is held constant in time, $T = T_w$, but variations in the streamwise direction are permitted, $T_w = T_w(x)$.

At the free-stream boundary ($y = y_{max}$), a decay condition is imposed on $v$, and the wall-normal derivative is set to zero for all other quantities. Therefore, the domain height has to be large enough so that all disturbances have decayed sufficiently and the imposed boundary condition does not influence the solution. The temperature is held constant, $T_\infty = 1$.

Near the outflow boundary, a damping region similar to the one proposed by Kloker, Konzelmann & Fasel (1993) is used. At the outflow boundary itself, all second derivatives are set to zero.

## 3. Numerical method

### 3.1. *Spatial discretization*

The derivatives in the $x$- and $y$-directions in the governing equations are discretized using fourth-order compact differences (Meitz 1996; Ferziger 1981). The grid points are equally spaced in the streamwise direction. In the wall-normal direction, a stretching function is used to cluster points near the wall (Anderson, Tannehill & Pletcher 1984),

$$\frac{y(j)}{y_{max}} = \frac{(\beta+1) - (\beta-1)\{[(\beta+1)/(\beta-1)]^{1-(j-1)/(M_y-1)}\}}{[(\beta+1)/(\beta-1)]^{1-(j-1)/(M_y-1)} + 1}, \tag{3.1}$$

where $j$ is the index of the grid point in the wall-normal direction, with $j = 1$ at the wall and $j = M_y$ at the free stream. $\beta$ is the parameter to control the distribution of grid points: $\beta \to 1^+$ clusters all points near the wall, $\beta \to \infty$ results in an equidistant grid.

The grid stretching is incorporated into the coefficients of the scheme, i.e. no mapping from a computational grid (with constant spacing) to the physical grid (with

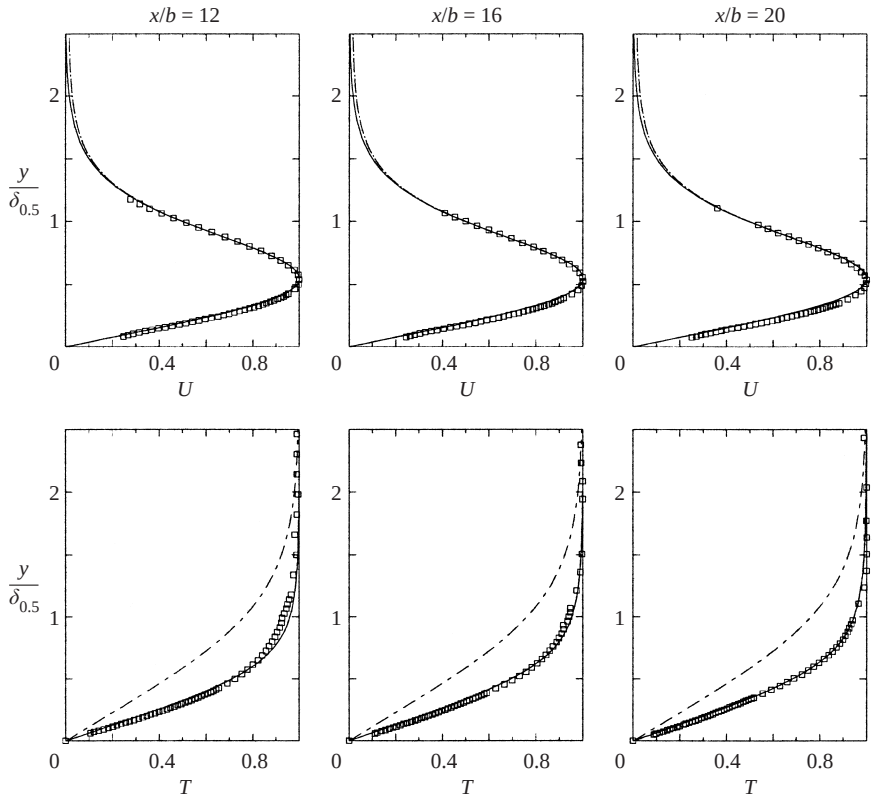


FIGURE 2. Comparison of the base flow computed with constant (· · ·) and temperature-dependent (– – –) $\nu$ and $\kappa$. Experimental results (□) and the similarity solution (—) are shown for comparison, together with the similarity solution without unheated starting length (—·—).

stretched coordinates) is necessary. Meitz & Fasel (2000) showed that this approach, while more tedious, yields higher accuracy compared to the method of coordinate transformation.

The streamwise derivatives are approximated using upwind and downwind biased difference schemes at successive Runge–Kutta substeps used for time integration. This improves numerical accuracy and stability without increasing the computational effort. To avoid the emergence of grid mesh oscillations in the streamwise direction, the vorticity field is filtered using a five-point compact difference filter (Lele 1992).

### 3.2. *Time integration*

For the time integration of the vorticity transport equations and the energy equation, a standard four-step explicit Runge–Kutta method (Ferziger 1981) is used.

At each Runge–Kutta substep, the computation proceeds as follows: first, the vorticity transport equation (2.1) and the energy equation (2.5) are integrated over one substep; next, the velocity Poisson equations (2.4) are solved in the order given. From the calculated velocities, the wall vorticity components are calculated (Meitz & Fasel 2000).

The numerical procedure outlined above has been used extensively by Meitz (1996) and Wernz & Fasel (1996, 1997) for the investigation of boundary layer and wall jet transition. For the computations presented here, a grid with $201 \times 100$ points has

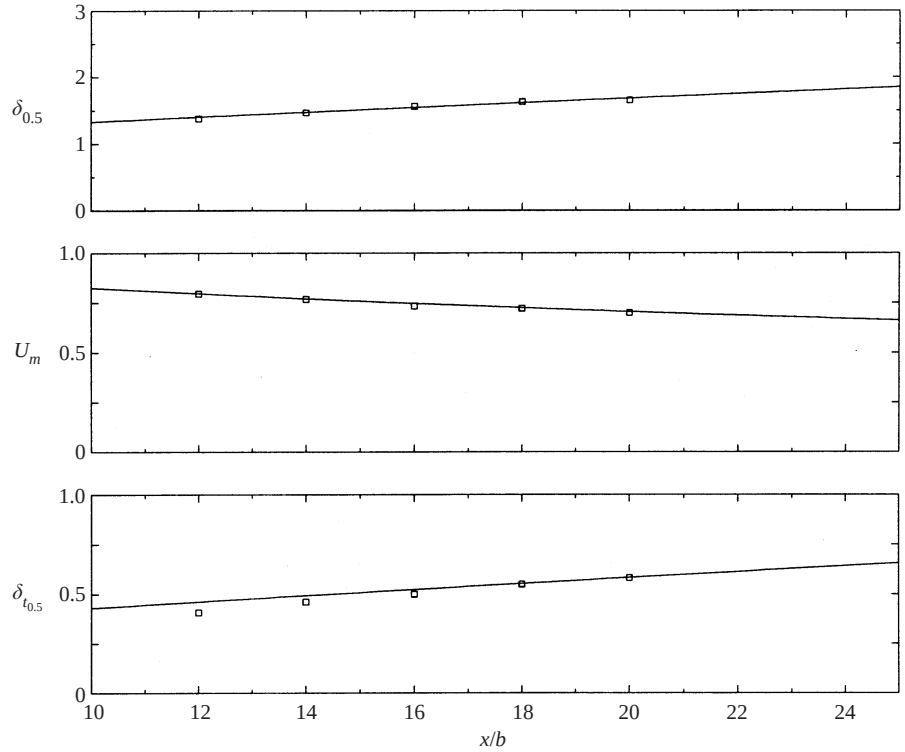


FIGURE 3. Comparison of the computed base flow (—) with experimental results (□). The graphs show the jet half-width $\delta_{0.5}$, the local maximum velocity $U_m$, and the half-width of the temperature profile as a function of downstream location $x/b$.

been used ($\beta = 1.05$). The resulting grid spacing is $\mathrm{d}x = 0.25$, $\mathrm{d}y_{wall} = 0.0186$, and the domain size is $5 < x < 50$ ($x$ measured from the virtual origin), $y_{max} = 10$. With a timestep of $\mathrm{d}t = 0.0269$, the Courant–Friedrichs–Levy number is $CFL = \mathrm{d}t/\mathrm{d}x = 0.1076$.

## 4. Results

The calculations presented here were performed in a joint effort with theoretical and experimental investigations of laminar heated wall jets in air that were forced by periodic perturbations. The first results of the experimental investigation were published by Quintana *et al.* (1997). In the experiments, the wall jet exits at a velocity of $U_j = 1.5\,\mathrm{m\,s^{-1}}$ through a nozzle of width $b = 3.2\,\mathrm{mm}$ into a quiescent surrounding. The jet exit Reynolds number is $Re_j = U_j b/\nu = 320$. To investigate the effect of perturbations of the velocity field on the temperature distribution, a heated test surface was built into the bottom of a closed return wind tunnel. The heating starts downstream of the nozzle, thus creating an unheated starting length. Due to thermal conduction in the wall, the exact wall temperature upstream of the test surface was not known.

The simulations closely match the geometry and the flow parameters of the experimental setup. The temperature boundary conditions were chosen to match the experiments, $T_\infty = 296.55\,\mathrm{K}$ and $T_w = 1.03$ on the heated test surface. However, the

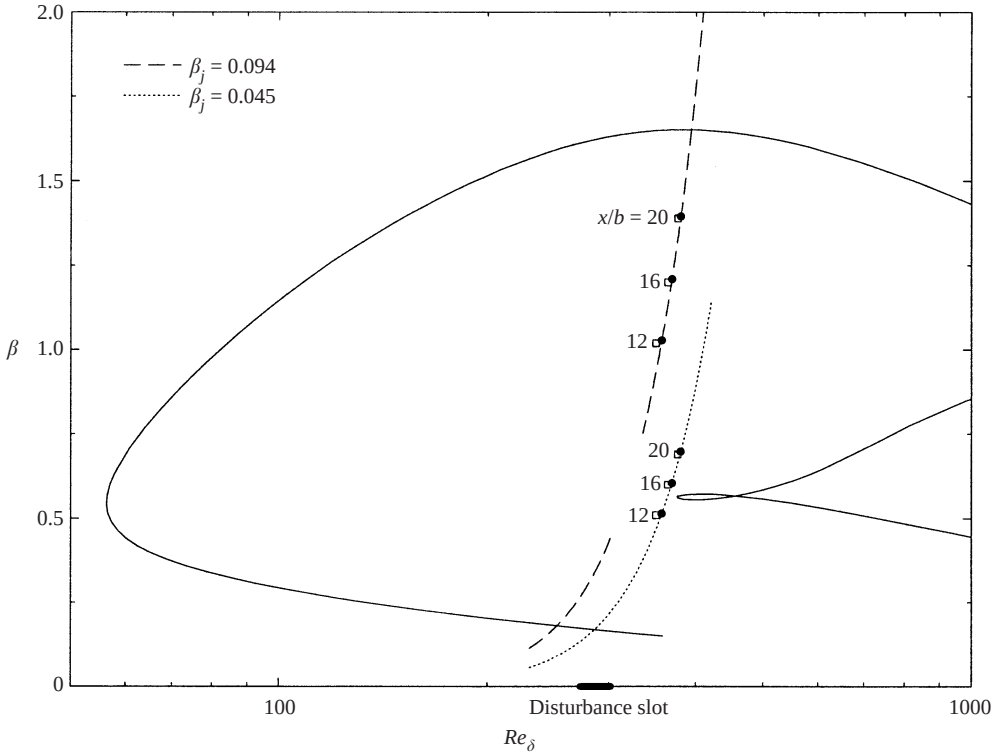


FIGURE 4. Linear stability diagram. $Re_\delta = u_{max}\delta_{0.5}/\nu$, $\beta_\delta = 2\pi F\delta_{0.5}/u_{max}$. □, The experimental measurement locations; ●, the corresponding locations in the computations.

effect of the unheated starting length had to be approximated. Numerous computations with different wall temperature distributions upstream of the test surface were performed to find the best agreement of the computational results and the measurements. To obtain comparable results using linear stability theory, the Prandtl number was adjusted to $Pr' = 1.4$ to match the thickness of the thermal boundary layer with the measurements.

The focus of this paper is on the early stages of transition, both in the linear and nonlinear regimes. These early stages of transition of the wall jet have been found by many authors to be predominantly two-dimensional (Bajura & Catalano 1975; Zhou *et al.* 1992; Wernz & Fasel 1996; Quintana 1997; Visbal, Gaitonde & Gogineni 1998).

### 4.1. *Base flow*

To assess the importance of the temperature dependence of the viscosity $\nu$ and the thermal conductivity $\kappa$, two sets of simulations were performed. In the first, both $\nu$ and $\kappa$ were held constant at a value corresponding to $T_\infty$, whereas in the second complete temperature dependence of $\nu$ and $\kappa$ was included in the calculation.

A comparison of the calculated base flows with the similarity solution (Glauert 1956; Likhachev & Tumin 1996) and the measurements is given in figure 2. The dotted and dashed lines represent the computed base flow for temperature dependent and independent $\nu$ and $\kappa$, respectively, and the solid line represents the similarity solution. The numerical results are obtained by solving the Navier–Stokes equations in a time-dependent fashion, however without the introduction of any time-dependent

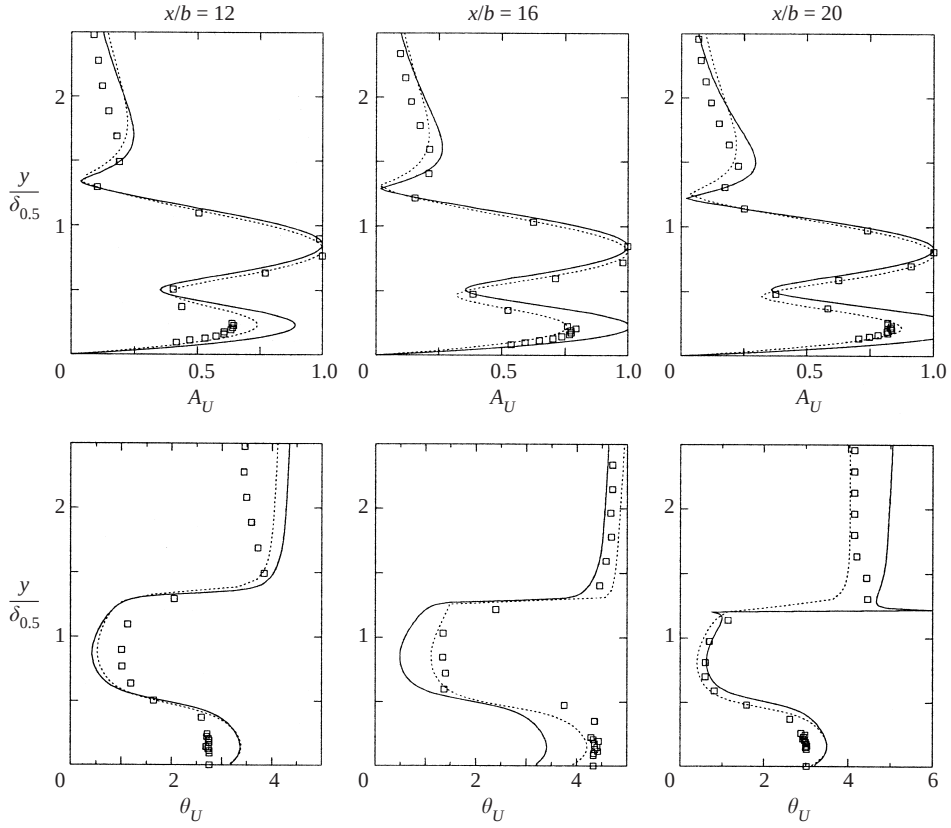


FIGURE 5. $u$-velocity amplitude and phase distribution, $\beta_j = 0.045$. Comparison of simulations ($\cdots$), experiments ($\square$), and linear stability theory results (—).

disturbances. After a small initial adjustment, the steady state is reached. The figure shows base flow profiles at three downstream locations, $x/b = 12, 16, 20$. The wall-normal coordinate $y$ is normalized using the local half-width $\delta_{0.5}$ (the distance from the wall in the outer shear layer where the velocity reaches one half the local maximum velocity). The $u$-velocity is normalized with the local maximum velocity, and the temperature is plotted as $T = (T - T_w)/(1 - T_w)$. At all three streamwise locations, excellent agreement between simulations, the similarity solution and experiments is achieved. Because of the small temperature difference between wall and free stream, the viscosity and thermal conductivity change by only about 2%, so that the $u$-velocity and the temperature profiles for both simulations, $\nu$, $\kappa$ constant and $\nu$, $\kappa$ variable, are virtually identical. To show the effect of the unheated starting length, the similarity solution of the energy equation (for constant wall temperature) is included in the graphs. Figure 3 shows the streamwise development of the jet half-width, $\delta_{0.5}$, the local maximum jet velocity, $U_m$, and the thickness of the temperature boundary layer, $\delta_{t_{0.5}}$ (defined as the $y$-location where $T = 0.5$). The agreement between experiments and computations is excellent, except for $\delta_{t_{0.5}}$ at $x/b = 12$, where the experimental value is about 10% lower than the computed value. This corresponds to the slight difference in the temperature profile (figure 2) at the first measurement location.

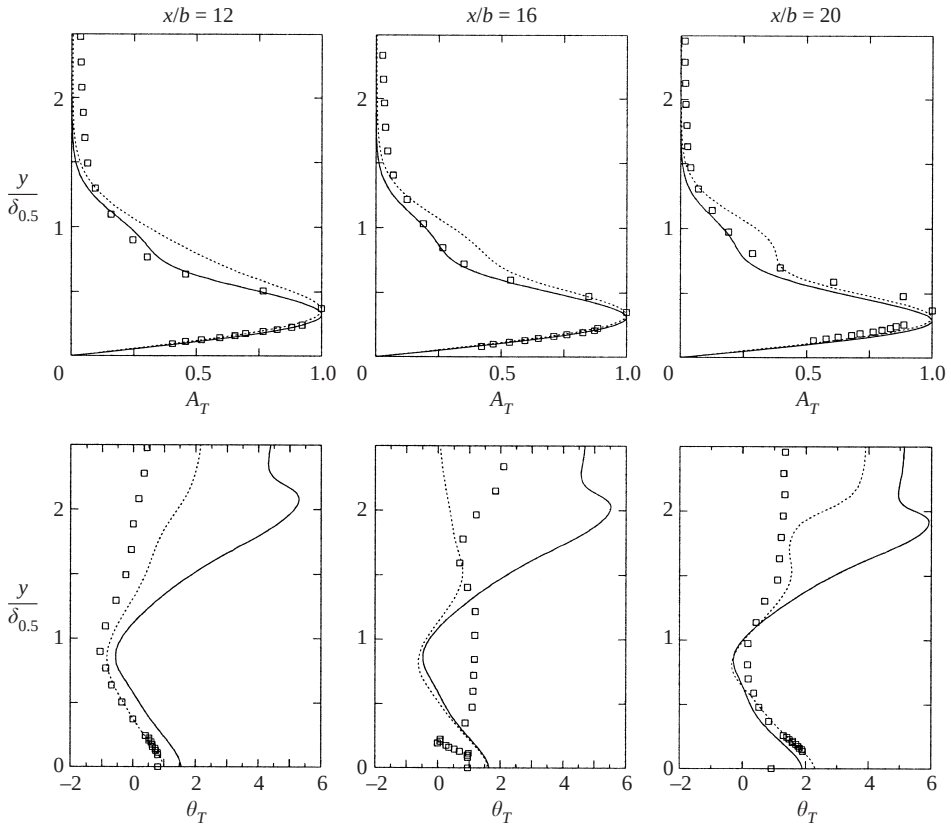


FIGURE 6. Temperature amplitude and phase distribution, $\beta_j = 0.045$. Comparison of simulations ($\cdots$), experiments ($\square$), and linear stability theory results (—).

### 4.2. *Small disturbance amplitudes*

For detailed investigations of the stability of the wall jet, disturbances of two different frequencies, $\beta_j = 0.045$ and $\beta_j = 0.094$ ($\beta_j = Fb/U_j$, $F$ is the forcing frequency in Hz), were introduced into an otherwise undisturbed wall jet flow (base flow). The calculated cases are shown in the stability diagram obtained from linear theory, figure 4. The line segments indicate the trajectory in the stability diagram as the downstream coordinate increases. The location of the inflow and outflow boundary as well as the location of the blowing and suction slot (disturbance input) is indicated in the stability diagram.

Qualitatively, the amplitude distribution can be viewed as a superposition of the eigenfunctions of a boundary layer near the wall and the free shear layer, extending from the velocity maximum outward.

To be able to compare the results of the simulations to results from linear stability theory as well as the experiments, the disturbance amplitude was chosen at a very low ($\hat{v} = 0.0005U_j$) level. In figures 5 and 6, the amplitude and phase distributions of the $u$ velocity and the temperature, as obtained from the simulations, are plotted for a forcing frequency of $\beta_j = 0.045$. Comparing the results of the simulation with the eigenfunction obtained from linear stability theory, the agreement is generally good. However, the magnitude of the near-wall peak of the velocity amplitude distribution

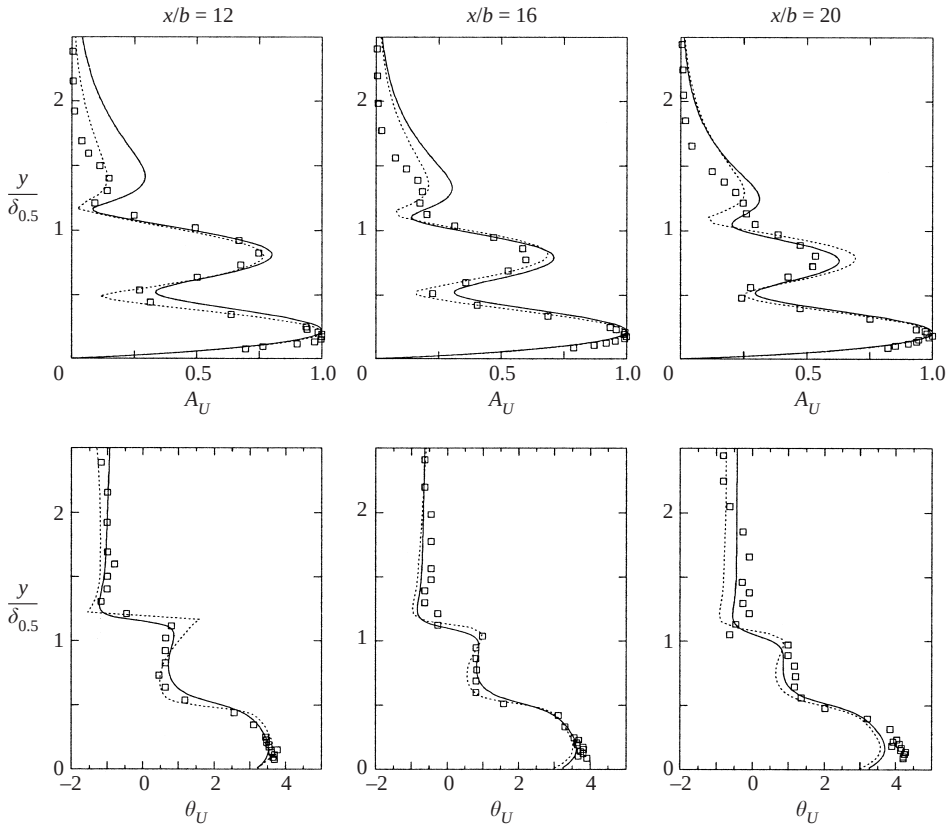


FIGURE 7. $u$-velocity amplitude and phase distribution, $\beta_j = 0.094$. Comparison of simulations ($\cdots$), experiments ($\square$), and linear stability theory results (—).

is overpredicted by linear theory. In fact, the experimental results also exhibit a lower inner maximum and in general agree very well with the results of the simulations. In figure 6, the temperature amplitude and phase distributions are shown for the same case. The agreement between simulations, linear theory and experiments is very good. The slight deviation of the results of the simulations from linear stability theory is most likely due to the small difference between the base flow profile used in the simulations and the temperature profile obtained from the similarity solution, showing the effect of the unknown temperature distribution upstream of the measurement locations (see figures 2 and 3).

Figure 7 shows a comparison of the calculated $u$-velocity amplitude and phase distribution to the eigenfunctions obtained from linear stability theory and the measurements for the case of $\beta_j = 0.094$. The agreement between the results of linear stability theory, experiment, and the simulation is very good.

The temperature amplitude and corresponding phase distributions are shown in figure 8. The agreement is not quite as good as for the velocity profiles. As can be seen from the base flow temperature profiles (figure 2), the largest deviation occurs at the $y$-location where the temperature gradient of the base flow changes the most. This in turn leads to the largest difference between measurements and DNS results. A possible explanation is that the upstream conduction in the wall of the experimental apparatus results in heating of the fluid in the nozzle, and, with the mixing in the

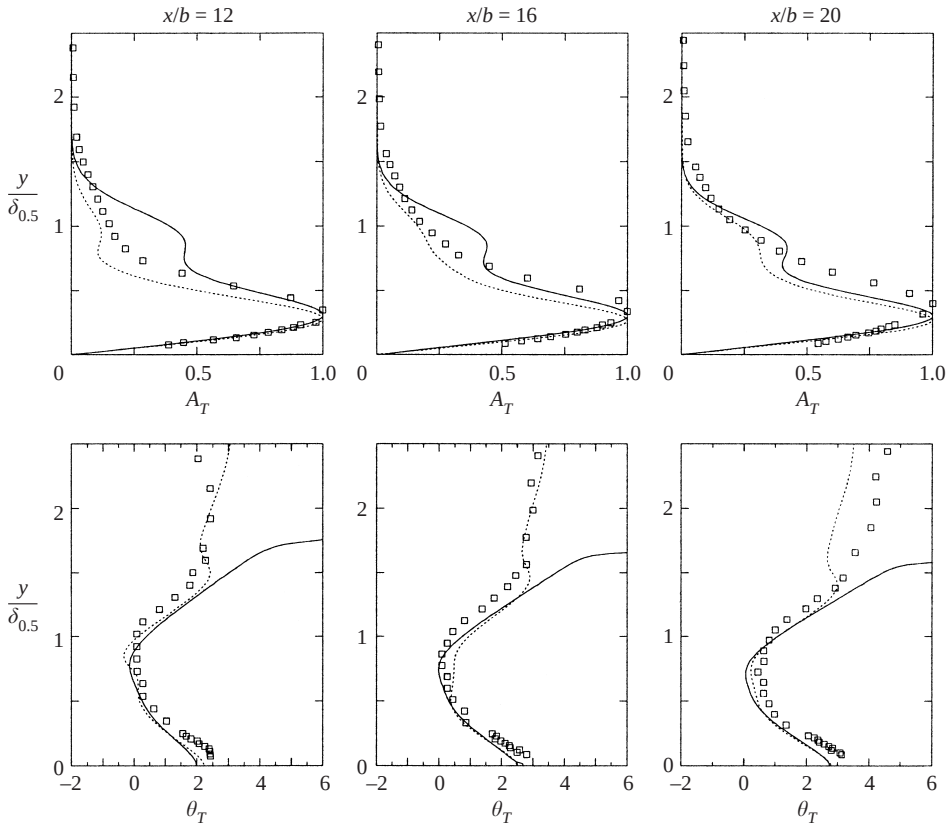


FIGURE 8. Temperature amplitude and phase distribution, $\beta_j = 0.094$. Comparison of simulations ($\cdots$), experiments ($\square$), and linear stability theory results (—).

| Case | $A_f/U_j$ | $A_s/U_j$ |
|---|---|---|
| Case01 | $5 \times 10^{-4}$ | — |
| Case02 | $1 \times 10^{-2}$ | — |
| Case03 | $1.5 \times 10^{-2}$ | — |
| Case04 | $1 \times 10^{-2}$ | $1 \times 10^{-3}$ |
| Case05 | $1 \times 10^{-2}$ | $1 \times 10^{-2}$ |
| Case06 | $1.5 \times 10^{-2}$ | $1 \times 10^{-3}$ |
| Case07 | $1.5 \times 10^{-2}$ | $5 \times 10^{-3}$ |

TABLE 1. Disturbance amplitudes of the fundamental ($A_f$) and the subharmonic ($A_s$) frequency for the large-amplitude cases. The fundamental frequency is either $\beta_j = 0.045$ or $\beta_j = 0.094$.

nozzle, in effectively heating the whole wall jet. This effect can only be captured if the upstream wall temperature distribution is known exactly.

### 4.3. *Large disturbance amplitudes*

#### 4.3.1. *Mean flow*

When the disturbance amplitude is increased, nonlinear effects become significant. Table 1 shows the forcing amplitudes of the different cases discussed below. The

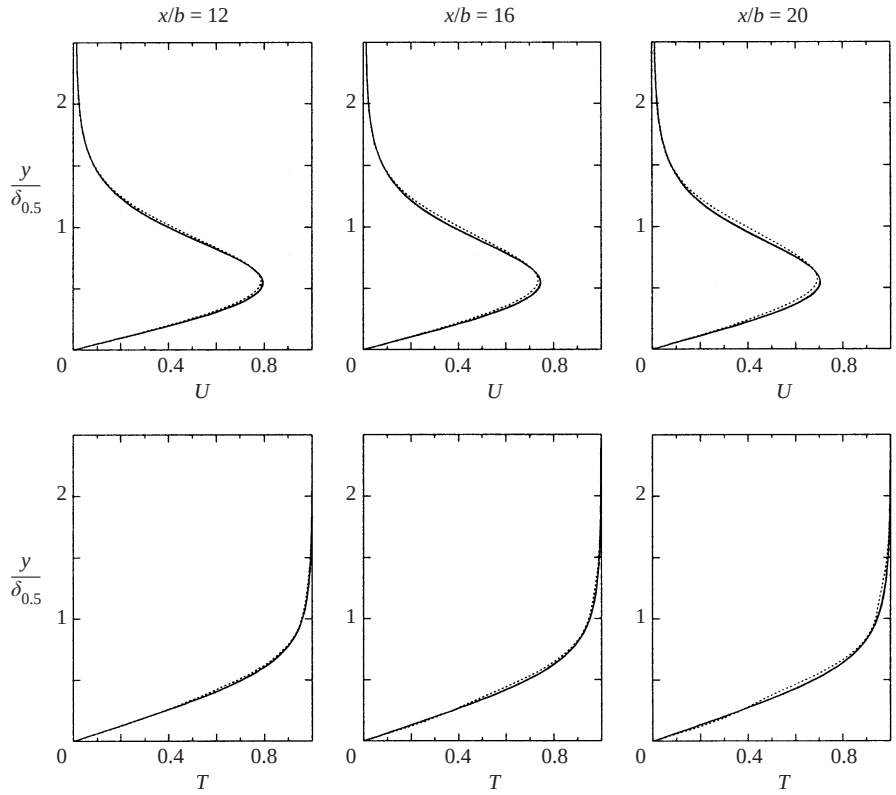


FIGURE 9. Comparison of mean flow distortion of $u$-velocity and temperature for different forcing amplitudes. $\beta_j = 0.045$. The dotted line shows the results when the forcing amplitudes are three times higher than in Case07.

effect of large-amplitude forcing on the mean flow is shown in figures 9–12. Unless noted otherwise, the wall-normal direction is normalized using the half-width of the undisturbed wall jet. At a frequency of $\beta_j = 0.045$, the forcing has no appreciable effect on the mean flow profiles (figure 9). This was first attributed to the fact that wall blowing and suction is not very efficient at this frequency but Quintana (1997) reported very similar results for a completely different forcing mechanism. Only when the amplitude levels are increased considerably (to three times the amplitudes of Case07), does a small distortion of the mean flow develop (figures 9 and 10).

For a frequency of $\beta_j = 0.094$, forcing at the smallest (linear) amplitude level has no appreciable effect on the mean flow. If the amplitudes are increased to $\hat{v} = 0.01U_j$ (Case02) and $\hat{v} = 0.015U_j$ (Case03), the mean flow starts to become distorted. First, the location of the maximum $u$-velocity is shifted away from the wall, thereby increasing the spreading rate of the wall jet (top of figures 11 and 12). Second, the maximum mean velocity decreases compared to the undisturbed base flow. Independent of the forcing frequency or amplitude (above a certain threshold), the wall shear stress, $\tau_w$, is reduced, figures 10 and 12.

The effect of high-amplitude forcing on the temperature distribution is shown at the bottom of figures 9–12. As for the velocity profiles, the effect of forcing at $\beta_j = 0.094$ is much more pronounced. With an increase in forcing amplitude, the mean

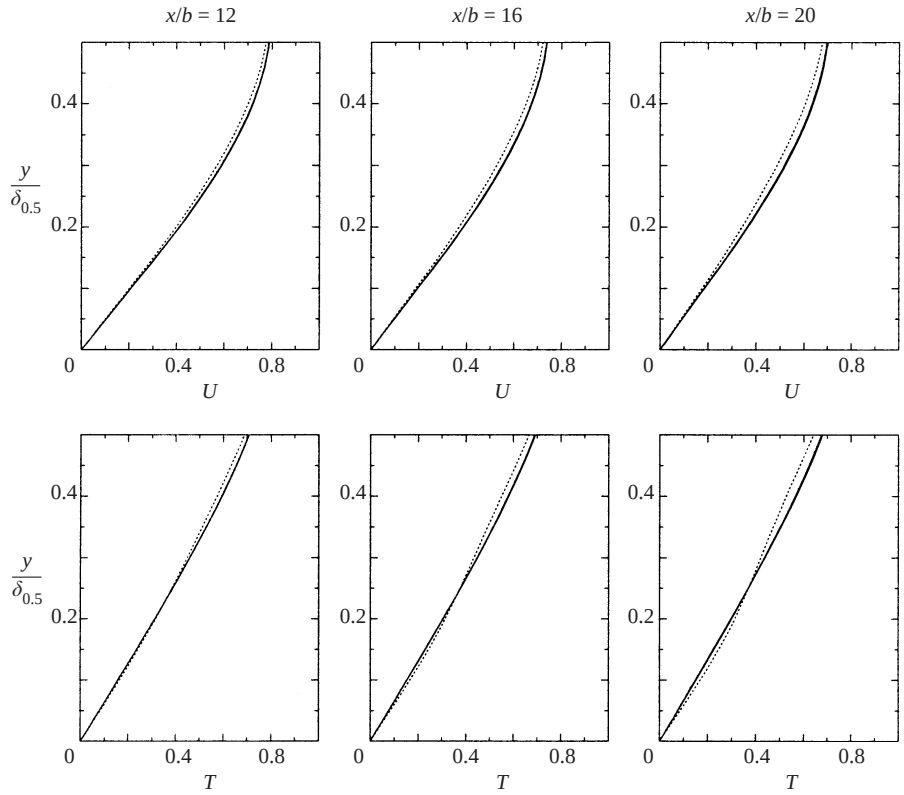


FIGURE 10. Comparison of mean flow distortion of $u$-velocity and temperature for different forcing amplitudes. $\beta_j = 0.045$. Near-wall region. The dotted line shows the results when the forcing amplitudes are three times higher than in Case07.

temperature profile develops an inflection point, which in turn yields an increase in wall heat transfer.

Both of these nonlinear effects can be observed more clearly in figure 13, where the normalized skin friction, $c_f = \partial u/\partial y|_{y=0}$, and the normalized wall heat transfer coefficient, $St = \partial T/\partial y|_{y=0}$, are plotted versus the streamwise coordinate $x$. For all but the smallest forcing amplitude, a strong deviation from the unforced case can be observed. In all cases, the wall shear is reduced, while the wall heat transfer is increased.

To emphasize this, figure 14 shows $2St/c_f$, the analogy factor, over the downstream distance $x$, for the case of $\beta_j = 0.094$. For the undisturbed case, the analogy factor decreases slightly in the streamwise direction. Far downstream, the analogy factor decreases to $(Pr')^{-2/3} \approx 0.8$. But when disturbances of high amplitude are introduced, the analogy factor increases sharply, showing an obvious deviation from the behaviour predicted by the Reynolds analogy. As can be seen from figure 13, both the reduction of the skin friction and the increase in the wall heat transfer contribute to the increase of the analogy factor. With increasing disturbance amplitude, the deviation from the undisturbed base flow occurs earlier and the difference between base flow and mean flow becomes larger. However, in contrast to the experimental results, the analogy factor does not increase in the whole domain. In fact, it decays downstream of $x/b = 19$ for Case02 and $x/b = 12$ for Case03.

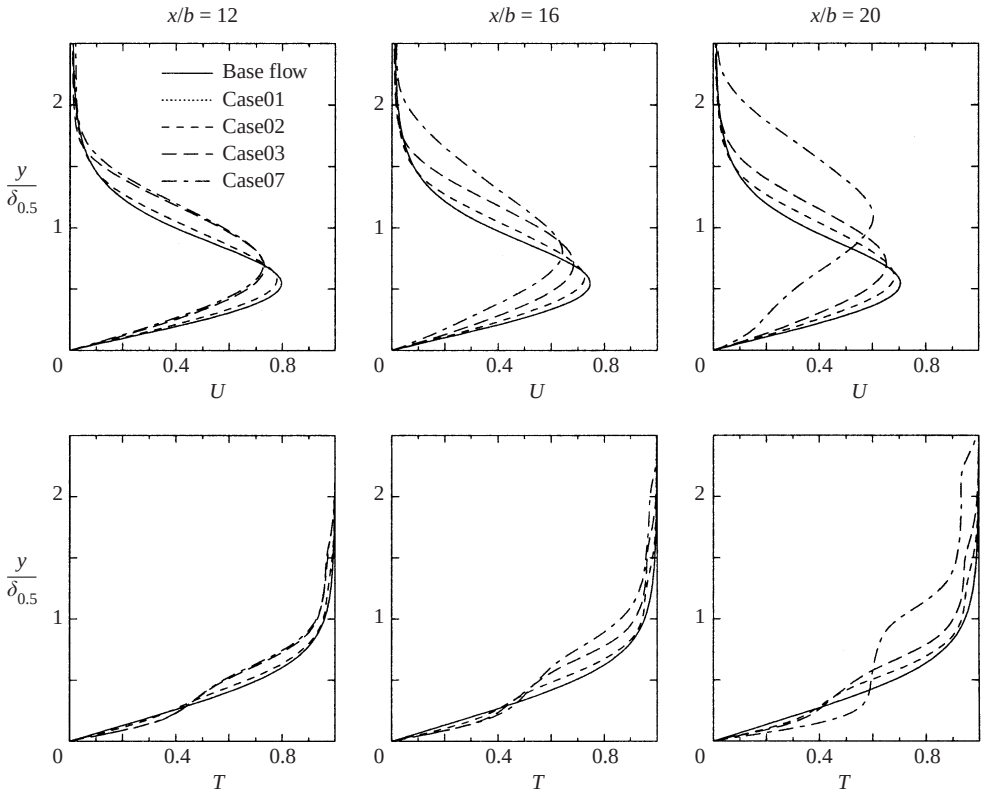


FIGURE 11. Comparison of mean flow distortion of $u$-velocity and temperature for different forcing amplitudes (see table 1). $\beta_j = 0.094$.

To investigate the cause of this difference between experiments and simulations, the power spectra of the experiments were scrutinized more closely. The experimental spectra indicate a subharmonic component with an initially small amplitude (the energy of the subharmonic is about 10% of the fundamental at $x/b = 12$). This subharmonic grows rapidly, and at the last measurement station, $x/b = 20$, the energy of the subharmonic is higher than that of the fundamental (Quintana 1997). This energy transfer from the fundamental to the subharmonic is a manifestation of the vortex pairing, which was observed by many authors (e.g. Bajura & Catalano 1975; Wernz & Fasel 1996) as discussed earlier. In the simulations described above, the flow was forced with only the fundamental frequency and the exclusion of the subharmonic prevented this energy transfer.

Therefore, in subsequent simulations, subharmonic forcing was added to the fundamental disturbance and the amplitude level of the subharmonic was varied (see table 1). High amplitudes of the subharmonic disturbances result in values of the analogy factor that are comparable with the experimental ones (figure 15). This is a clear indication that it is not the amplitude of the fundamental disturbance itself, but rather the subharmonic cascade that is responsible for the dramatic increase of the analogy factor. A comparison of Case03, Case06, and Case07 (figure 15), which differ only in the disturbance amplitude of the subharmonic, clearly demonstrates the role

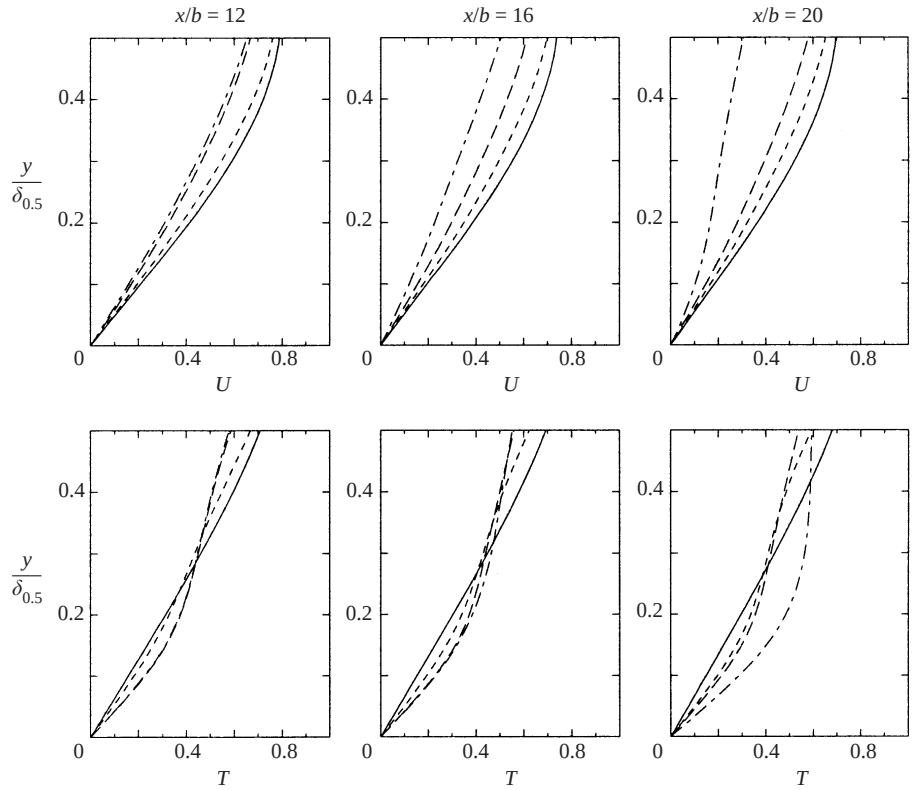


FIGURE 12. Comparison of mean flow distortion of $u$-velocity and temperature for different forcing amplitudes (see table 1). $\beta_j = 0.094$. Near-wall region. For legend, see figure 11.

of the subharmonic: the higher the amplitude of the subharmonic, the stronger the deviation of the analogy factor from the undisturbed case.

4.3.2. *Fluctuating quantities*

To clarify the role of the disturbance waves in the changes of the mean flow profiles shown in the preceding section, the time-dependent flow fields have to be examined.

The temporal average of the boundary layer form of the momentum and energy equations are

$$\frac{\partial \bar{u}}{\partial t} + \bar{u}\frac{\partial \bar{u}}{\partial x} + \bar{v}\frac{\partial \bar{u}}{\partial y} = \frac{\partial}{\partial y}\left[\frac{1}{Re}\frac{\partial \bar{u}}{\partial y} - \overline{u'v'}\right], \tag{4.1a}$$

$$\frac{\partial \bar{T}}{\partial t} + \bar{u}\frac{\partial \bar{T}}{\partial x} + \bar{v}\frac{\partial \bar{T}}{\partial y} = \frac{\partial}{\partial y}\left[\frac{1}{Pe}\frac{\partial \bar{T}}{\partial y} - \overline{v't'}\right], \tag{4.1b}$$

or, with the definitions of (1.2) and (1.3),

$$\frac{\partial \bar{u}}{\partial t} + \bar{u}\frac{\partial \bar{u}}{\partial x} + \bar{v}\frac{\partial \bar{u}}{\partial y} = \frac{\partial}{\partial y}\left[\left(\frac{1}{Re} + \nu_t\right)\frac{\partial \bar{u}}{\partial y}\right], \tag{4.2a}$$

$$\frac{\partial \bar{T}}{\partial t} + \bar{u}\frac{\partial \bar{T}}{\partial x} + \bar{v}\frac{\partial \bar{T}}{\partial y} = \frac{\partial}{\partial y}\left[\left(\frac{1}{Pe} + \kappa_t\right)\frac{\partial \bar{T}}{\partial y}\right]. \tag{4.2b}$$

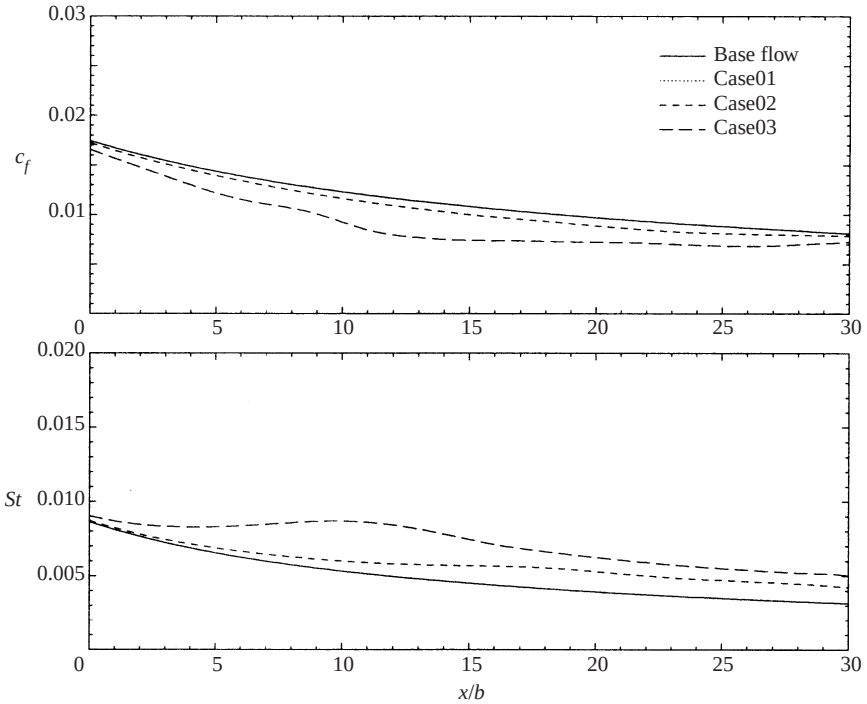


FIGURE 13. Skin friction coefficient $c_f$ and wall heat transfer coefficient $St$ for $\beta_j = 0.094$. See table 1 for an explanation of the different cases.

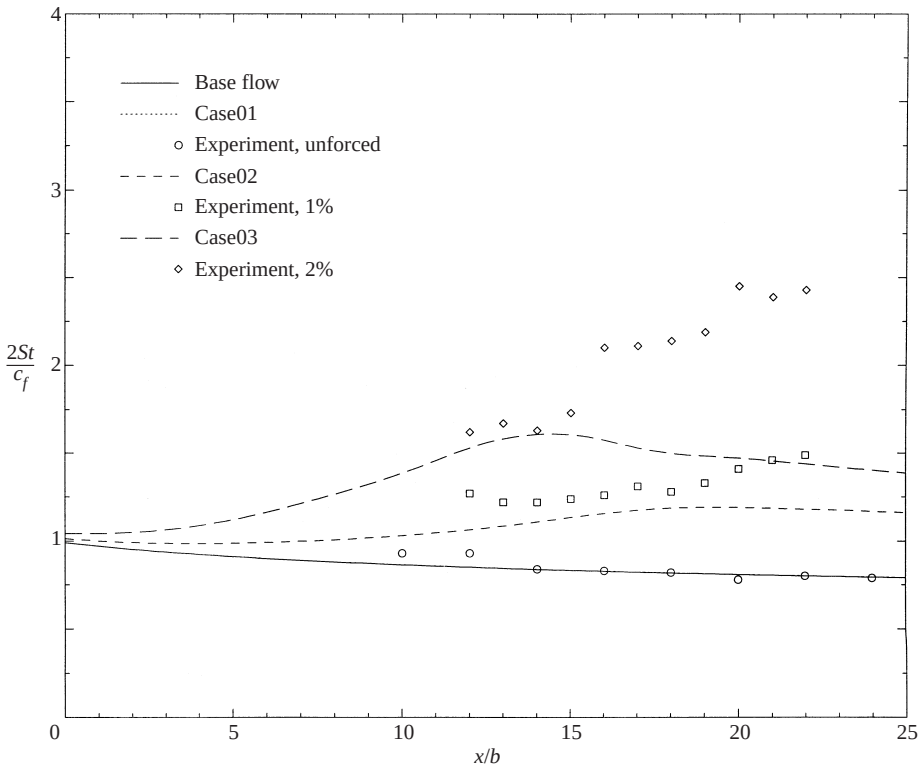


FIGURE 14. Analogy factor, $2St/c_f$, for $\beta_j = 0.094$. See table 1 for an explanation of the different cases. The forcing level of the experiments is defined as $|(u'_{max})|/U_j$ of the fundamental disturbance at the nozzle exit plane.

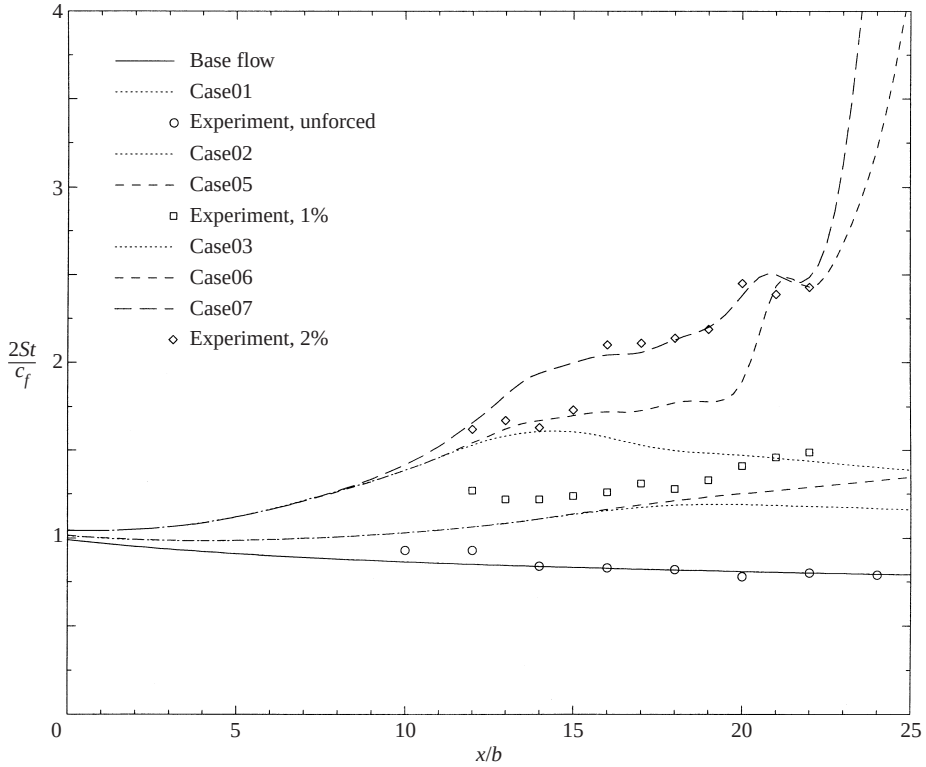


FIGURE 15. Analogy factor, $\beta_j = 0.094$. See table 1 for an explanation of the different cases.

The top three graphs in figure 16 show a comparison of the Reynolds stress distribution obtained from the simulations, the experiments and linear theory. The experimental data show a peak near $y/\delta_{0.5} = 0.4$, which is also present in the computational results at $x/b = 12$. In the computations, however, this peak decays rapidly in the downstream direction. At the last measurement station, $x/b = 20$, the agreement between results from linear theory and simulations is excellent. The difference to the experimental results is possibly due to inaccuracies in the determination of $v'$ from the measured $u'$-distribution (Quintana 1997). The top graphs in figures 17–19 show the distribution of $\overline{u'v'}$ in the wall-normal direction $y$ for Case01, Case03, and Case06. The velocity profiles of the undisturbed base flow and the mean flow are included in the figures for comparison.

From the momentum equation (4.2*a*), the effect of $\overline{u'v'}$ is equivalent to a local increase in viscosity. According to the Prandtl mixing length hypothesis, this corresponds to a reduction of the velocity gradient wherever $\overline{u'v'}$ is large, a trend that can be observed in figures 17–19. It is interesting to note that even for a forced laminar wall jet the Boussinesq approximation, $\overline{u'v'} = f(\mathrm{d}u/\mathrm{d}y)$, especially $\overline{u'v'} = 0$ where $(\mathrm{d}u/\mathrm{d}y) = 0$, does not hold, a well-known characteristic of turbulent wall jets (Launder & Rodi 1983).

To qualitatively analyse the effect of the forcing on the temperature field, the location and size of the large structures, identified using the $\lambda_2 < 0$ criterion Jeong & Hussain 1995, is plotted and compared to the instantaneous temperature field. In figure 20(*a*), the temperature field of the undisturbed base flow is shown in grey scale

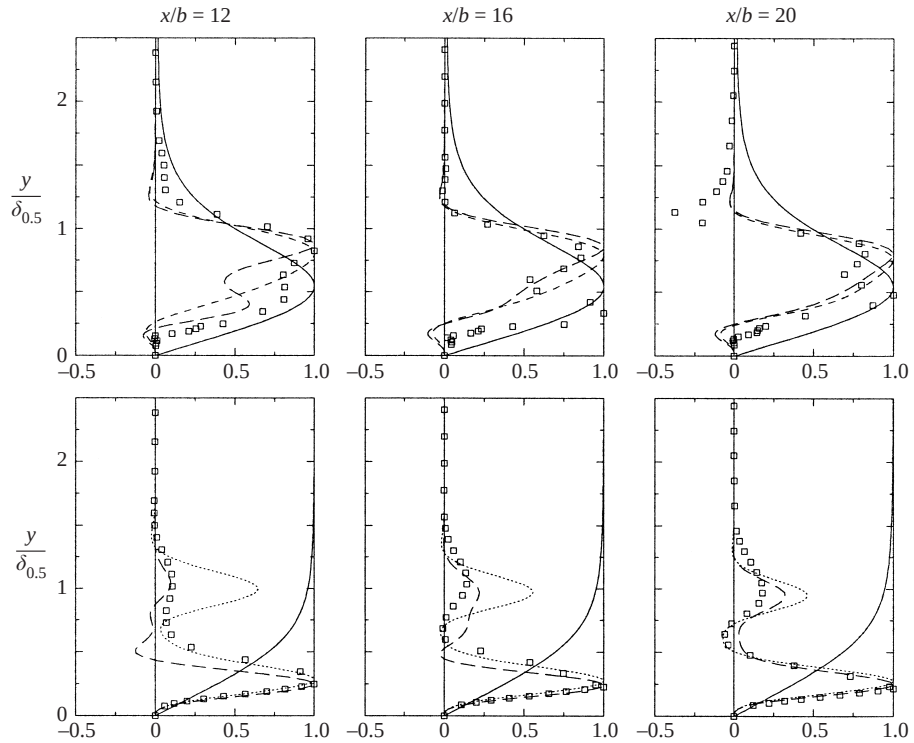


FIGURE 16. Normalized $\overline{u'v'}$ (top) and $\overline{v't'}$ (bottom), Case01, $\beta_j = 0.094$. Comparison of simulations (– – –), linear theory (···), and experiment (□). Base flow profiles are shown for comparison. Experimental data from Quintana (1997).

for comparison. Note that the spatial coordinates are scaled with the global length scale $b$ (the nozzle height in the experiments), so the growth of the jet width in the downstream direction becomes apparent. If only single-frequency disturbances are introduced, figure 20($b$), a very regular, staggered pattern of vortices develops, as was observed previously by Wernz & Fasel (1996).

The temperature field is governed by the local, unsteady convection. With the developing vortical disturbances, the temperature field is altered significantly when compared to the undisturbed base flow. Qualitatively speaking, the structures near the wall turn clockwise, transporting high-temperature fluid away from the wall on the upstream side, while convecting colder ambient fluid towards the wall on the downstream side. The outer row of vortices, turning counterclockwise, enhance this flow pattern by entraining cold ambient fluid on their upstream side. Inside the vortical structures, the instantaneous temperature gradient $\partial T/\partial y$ can become positive, locally leading to a reversal of the heat flux (now toward the wall). This effect is more pronounced for the inner row of vortices.

If, in addition, a disturbance with half the frequency (subharmonic) is introduced, vortex pairing occurs. For high enough amplitudes of the subharmonic, figures 20($c$) and 20($d$), the subharmonic disturbances dominate the flow. With increasing amplitude level, the location of the pairing process is moved upstream.

With the growth of the subharmonic (i.e. a halving of the fundamental frequency), the length scale doubles, and the vortices extend further into the ambient fluid. This

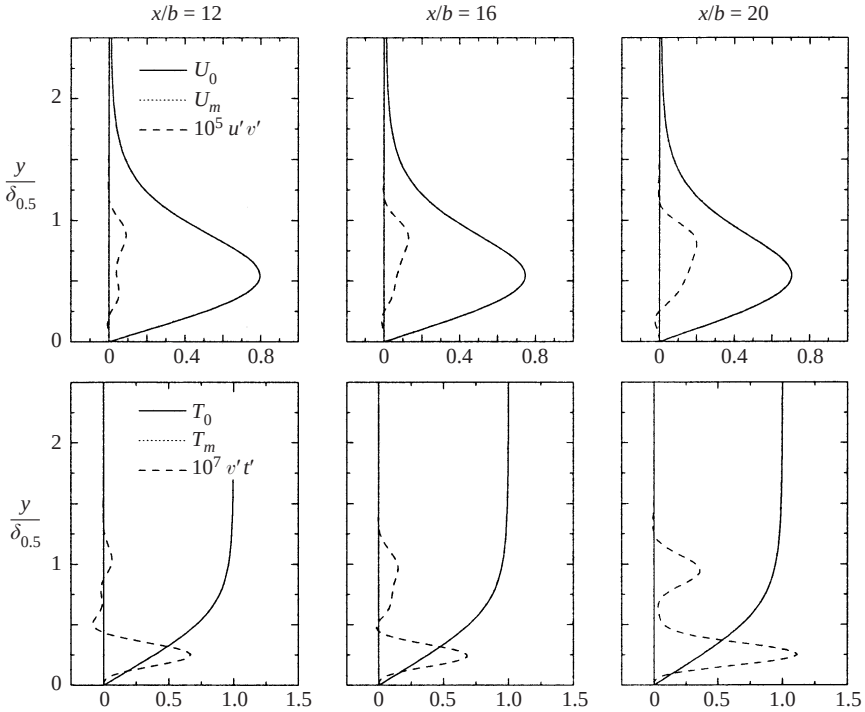


FIGURE 17. Scaled $\overline{u'v'}$ (top) and $\overline{v't'}$ (bottom), Case01, $\beta_j = 0.094$. Velocity profiles $u_0$ (base flow) and $u_m$ (mean flow) are shown for comparison.

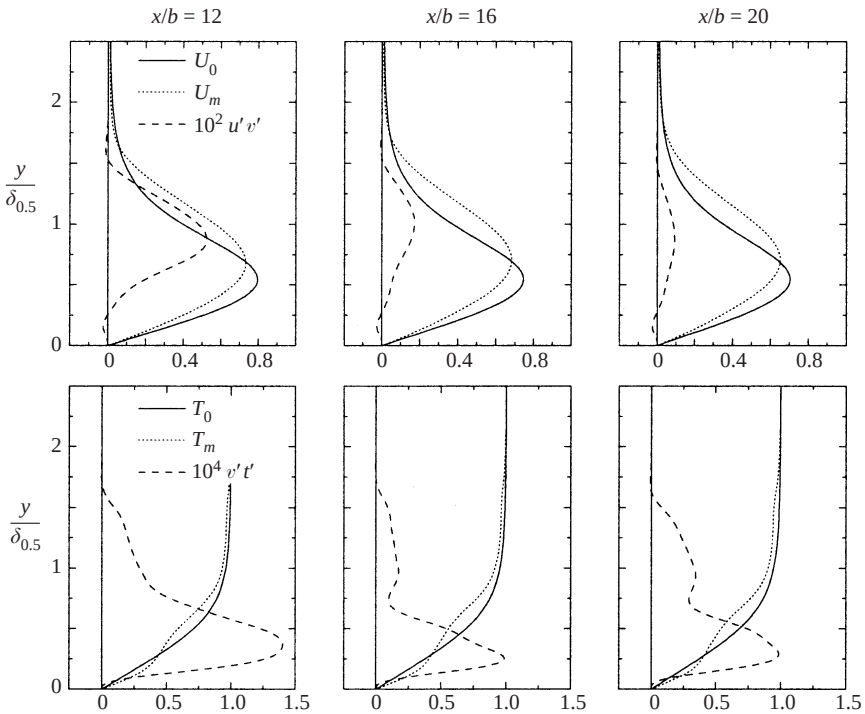


FIGURE 18. $\overline{u'v'}$ and $\overline{v't'}$, Case03, $\beta_j = 0.094$. Note the change of scale of $\overline{u'v'}$ compared to figure 17.

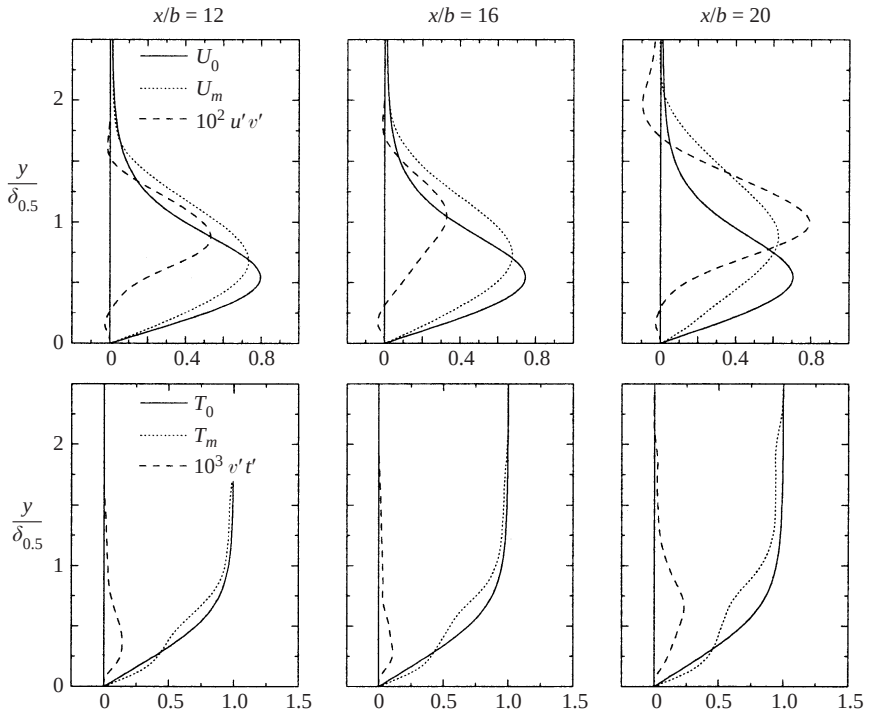


FIGURE 19. $\overline{u'v'}$ and $\overline{v't'}$, Case06, $\beta_j = 0.094$.

results in a rapid growth of the wall jet thickness (see figure 11), and a corresponding growth of the thermal boundary layer thickness. As can be seen in figures 20(*c*) and 20(*d*) at $x/b = 17$, local pockets of cold fluid develop instantaneously, leading to very large temperature gradients near the wall. This very high localized heat transfer rate leads to an increase in the average heat transfer from the wall, which manifests itself in the distortion of the mean temperature profiles (see figure 12).

To gain a better understanding of these processes, the eddy thermal diffusivity, commonly used in the analysis of turbulent flows, is utilized to analyse the unsteady flow field. Since small, turbulent scales are not present in the simulations, the effect of the large-scale instability waves is captured by $\overline{v't'}$, the correlation between normal velocity and temperature disturbances. In the bottom graphs of figures 17–19 $\overline{v't'}$ as a function of $y/\delta_{0.5}$ is shown, together with the mean temperature profile and the undisturbed base flow; $v'$ and $t'$ are taken as $f' = f - f_0$, i.e. all unsteady Fourier components combined. All plots are for a fundamental frequency of $\beta_j = 0.094$.

From the energy equation (4.2*b*), the heat transfer through a unit area parallel to the wall is the sum of thermal conduction and the eddy heat flux,

$$q_y = -\frac{1}{Pe}\frac{\partial T}{\partial y} + \overline{v't'}. \tag{4.3}$$

In figure 16, the bottom graphs show a comparison of $\overline{v't'}$ for the linear case. Consistent with the findings for the temperature base flow (figure 2) and disturbance amplitude distributions (figure 8), the results of the simulations and linear theory agree very well at $x/b = 20$, except in the outer region of the wall jet, where the

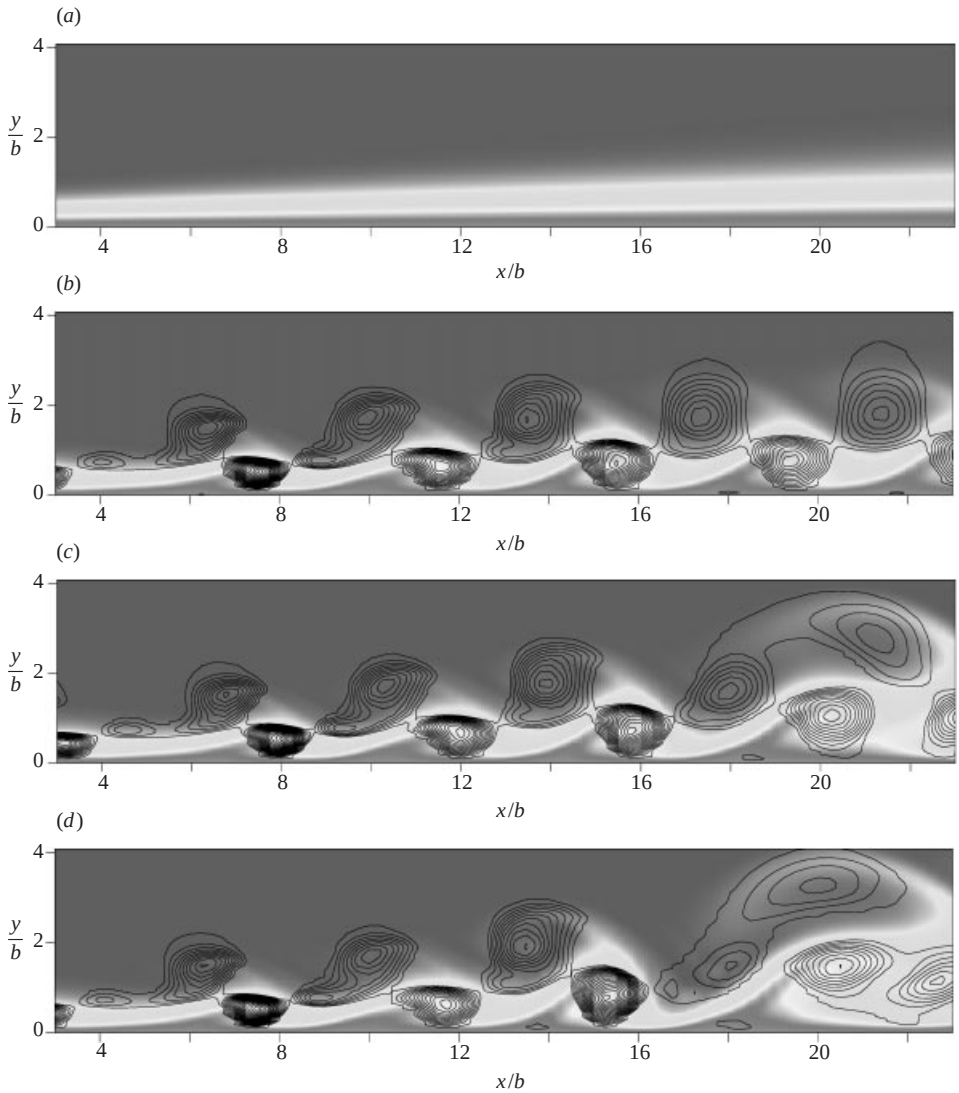


FIGURE 20. Instantaneous temperature distribution and structures in the flow field. Downstream distance $x$ and wall normal distance $y$ are scaled with the jet nozzle height $b$. Contour lines show the instantaneous location of vortices (identified using the $\lambda_2 < 0$ criterion of Jeong & Hussain 1995). (*a*) Undisturbed base flow, (*b*) Case03, (*c*) Case06, (*d*) Case07.

linear theory predicts a higher secondary peak in $\overline{v't'}$. Comparing the results to the measurements shows fairly good agreement.

As seen in figure 18, $\overline{v't'}$ has a local maximum at the $y$-location where the inflection point in the mean temperature profile develops (note the difference in the scale of $\overline{v't'}$). The increase in the forcing amplitude affects mainly the peak of $\overline{v't'}$ near $y/\delta_{0.5} = 1$, which is reduced in relative magnitude. In Case03, a second weak peak develops near $y/\delta_{0.5} = 0.6$, which is even more pronounced in Case05 and Case06, resulting in an almost constant temperature distribution between $y/\delta_{0.5} = 0.3$ and $y/\delta_{0.5} = 0.5$.

The strong correlation of the $y$-location of the increase in $\overline{v't'}$ and the reduction of

$\partial T/\partial y$ suggests that the large structures captured by $\overline{v't'}$ indeed are the main source for the large mean flow distortion and the development of the inflection point in the mean temperature profile.

## 5. Conclusion

The effect of two-dimensional forcing on a laminar wall jet with heat transfer has been investigated using direct numerical simulations. For the simulations, highly accurate time and space discretization schemes were employed. The simulation code was validated by comparison of the computational results with linear stability theory.

The flow was forced with frequencies $\beta_j = 0.045$, and $\beta_j = 0.094$. Forcing with $\beta_j = 0.045$ had no significant influence on the mean velocity and temperature profiles. At very high disturbance amplitude levels ($v' = 0.01U_0$), a slight decrease in wall shear stress and a small increase in wall heat transfer was found.

Significant changes of the mean flow were observed when forcing with $\beta_j = 0.094$. For very low disturbance amplitudes, the simulations show very good agreement with results from linear stability theory. Increasing the amplitude leads to a strong nonlinear distortion of the mean flow which was also observed in experiments. The skin friction is reduced markedly, the local maximum velocity is decreased, and the wall heat transfer is increased. It was shown that the large structures, generated by introducing periodic disturbances into the flow (by blowing/suction at the wall), are indeed the main cause for the strong mean flow distortion of both velocity and temperature.

Forcing introduces two staggered rows of vortical disturbances. At high amplitudes, these structures increase the mixing within the wall jet (as shown by the maximum in the Reynolds stress distribution), which increases the spreading rate and reduces the skin friction. In addition, the large structures entrain cold fluid from the ambient, and hot fluid is convected away from the wall, which leads to an increase in the effective thermal diffusion. Locally, the highly unsteady flow field leads to the development of very high wall temperature gradients and in the mean to an inflection point in the temperature profile and an increase in the wall heat transfer.

This work was supported by the Department of Energy under contract 93-ER-14396.

## REFERENCES

Akatnov, N. I. 1953 Development of two-dimensional laminar incompressible jet near a rigid wall. *Proc. Leningrad Polytec. Inst.* **5**, 24–31.

Amitay, M. 1994 Theoretical and experimental investigations of a laminar two-dimensional wall jet. PhD thesis, Faculty of Aerospace Engineering, Technion, Israel.

Amitay, M. & Cohen, J. 1993 The mean flow of a laminar walljet subjected to blowing or suction. *Phys. Fluids* A **5**, 2053–2057.

Amitay, M. & Cohen, J. 1997 Instability of a two-dimensional plane wall jet subjected to blowing or suction. *J. Fluid Mech.* **344**, 67–94.

Anderson, D. A., Tannehill, J. C. & Pletcher, R. H. 1984 *Computational Fluid Mechancis and Heat Transfer*. McGraw-Hill.

Bajura, R. A. & Catalano, M. R. 1975 Transition in a two-dimensional plane wall jet. *J. Fluid Mech.* **70**, 773–799.

Bajura, R. A. & Szewezyk, A. A. 1970 Experimental investigation of a laminar two-dimensional plane wall jet. *Phys. Fluids* **13**, 1653–1664.

Bertolotti, F. 1991 Linear and nonlinear stability of boundary layers with streamwise varying properties. PhD thesis, Ohio State University.

Chun, D. H. & Schwarz, W. H. 1967 Stability of the plane incompressible viscous wall jet subjected to small disturbances. *Phys. Fluids* **10**, 911–915.

Cohen, J., Amitay, M. & Bayly, B. J. 1992 Laminar-turbulent transition of wall jet flows subjected to blowing and suction. *Phys. Fluids* **4**, 283–289.

Dec, J. E. & Keller, J. O. 1990 Time-resolved gas temperatures in the oscillating turbulent flow of a pulse combustor tail pipe. *Combust. Flame* **80**, 358–370.

Fasel, H., Rist, U. & Konzelmann, U. 1990 Numerical investigation of the three dimensional development in boundary layer transition. *AIAA J.* **28**, 29–37.

Ferziger, J. H. 1981 *Numerical Methods for Engineering Application.* Wiley.

Glauert, M. B. 1956 The wall jet. *J. Fluid Mech.* **1**, 625–643.

Gogineni, S., Visbal, M. & Shih, C. 1997 Experimental and numerical investigation of transitional plane wall jet. *AIAA Paper* 97-0071.

Gorla, R. S. R. & Jeng, D. R. 1971 Laminar plane wall jet. *Proc. 12th Midwestern Conf.: Developments in Mechanics*, vol. 6, pp. 137–151.

Holmberg, D. G. & Pestian, D. J. 1996 Wall-jet turbulent boundary layer heat flux, velocity, and temperature spectra and time scales. *Intl Gas Turbine Conf. Birmingham, UK. ASME Paper* 96-GT-529.

Jeong, J. & Hussain, F. 1995 On the identification of a vortex. *J. Fluid Mech.* **285**, 69–94.

Kloker, M., Konzelmann, U. & Fasel, H. 1993 Outflow boundary conditions for spatial navier-stokes simulations of transitional boundary layers. *AIAA J.* **31**, 620–628.

Launder, B. E. & Rodi, W. 1983 The turbulent wall jet – measurements and modeling. *Ann. Rev. Fluid Mech* **15**, 429–459.

Lele, S. K. 1992 Compact finite difference schemes with spectral-like resolution. *J. Comput. Phys.* **103**, 16–42.

Likhachev, O., Quintana, D. L. & Wygnanski, I. 1998 On the stability of a laminar wall jet with heat transfer. *J. Flow Turbulence and Combustion* (Submitted).

Likhachev, O. & Tumin, A. 1996 Stability of a compressible laminar wall jet with heat transfer. *Trans. ASME*: *J. Fluids Engng* **118**.

Meitz, H. 1996 Numerical investigation of suction in a transitional flat-plate boundary layer. PhD thesis, The University of Arizona.

Meitz, H. & Fasel, H. F. 2000 A compact-difference scheme for the navier-stokes equations in vorticity-velocity formulation. *J. Comput. Phys.* **157**, 371–403.

Mele, P., Morganti, M., Scibillia, M. F. & Lasek, A. 1986 Behavior of wall jet in laminar-to-turbulent transition. *AIAA J.* **24**, 938–939.

Quintana, D. L. 1997 Augmentation of heat transfer in a laminar wall jet by selective forcing. PhD thesis, The University of Arizona.

Quintana, D. L., Amitay, M., Ortega, A. & Wygnanski, I. J. 1997 Heat transfer in the forced laminar wall jet. *J. Heat Transfer* **119**, 451–459.

Schwarz, W. H. & Caswell, B. 1961 Some heat transfer characteristic of the two-dimensional laminar incompressible wall jet. *Chem. Engng Sci.* **16**, 338–351.

Tetervin, N. 1948 Laminar flow of a slightly viscous incompressible fluid that issues from a slit and passes over a flat plate. *NACA TN*. 1644.

Tsuji, Y., Morikawa, Y., Nagatani, T. & Sakou, M. 1977 The stability of a two-dimensional wall jet. *Aero. Q.* **28**, 235–246.

Visbal, M. R., Gaitonde, D. V. & Gogineni, S. P. 1998 Direct numerical simulation of a forced transitional plane wall jet. *AIAA Paper* 98-2643.

Wernz, S. 1993 Stability investigations of a laminar wall jet using the linear stability theory. Master's thesis, The University of Arizona.

Wernz, S. & Fasel, H. F. 1996 Numerical investigation of unsteady phenomena in wall jets. *AIAA Paper* 96-0079.

Wernz, S. & Fasel, H. F. 1997 Numerical investigation of forced transitional wall jets. *AIAA Paper* 97-2022.

Zhou, M. D., Rothstein, J. & Wygnanski, I. 1992 On the hydrodynamic stability of the wall jet. *Eleventh Australasian Fluid Mechanics Conf., Hobart, Australia* (ed. M. R. Davis & G. J. Walker). Printed at the University of Tasmania.